

Characterization of proton irradiated 3D-DDTC pixel sensor prototypes fabricated at FBK

A. La Rosa^{a,*}, M. Boscardin^b, M. Cobal^c, G.-F. Dalla Betta^d, C. Da Vià^e, G. Darbo^f, C. Gallrapp^a, C. Gemme^f, F. Huegging^g, J. Janssen^g, A. Micelli^c, H. Pernegger^a, M. Povoli^d, N. Wermes^g, N. Zorzi^b

^aCERN, Geneva 23, CH-1211, Switzerland

^bFondazione Bruno Kessler, FBK-CMM, Via Sommarive 18, I-38123 Trento, Italy

^cUniversità degli Studi di Udine and INFN Trieste, Gruppo Collegato di Udine, Via delle Scienze 208, I-33100 Udine, Italy

^dDISI, Università degli Studi di Trento and INFN Padova, Gruppo Collegato di Trento, Via Sommarive 14, I-38123 Trento, Italy

^eSchool of Physics and Astronomy, University of Manchester, Oxford Road, Manchester, M13 9PL, United Kingdom

^fINFN Sezione di Genova, Via Dodecaneso 33, I-14146 Genova, Italy

^gPhysikalisches Institut, Universität Bonn, Nußallee 12, D-53115 Bonn, Germany

Abstract

In this paper we discuss results relevant to 3D Double-Side Double Type Column (3D-DDTC) pixel sensors fabricated at FBK (Trento, Italy) and oriented to the ATLAS upgrade. Some assemblies of these sensors featuring different columnar electrode configurations (2, 3, or 4 columns per pixel) and coupled to the ATLAS FEI3 read-out chip were irradiated up to large proton fluences and tested in laboratory with radioactive sources. In spite of the non optimized columnar electrode overlap, sensors exhibit reasonably good charge collection properties up to an irradiation fluence of $2 \times 10^{15} \text{ n}_{\text{eq}}\text{cm}^{-2}$, while requiring bias voltages in the order of 100 V. Sensor operation is further investigated by means of TCAD simulations which can effectively explain the basic mechanisms responsible for charge loss after irradiation.

1. Introduction

The fast increase in luminosity in the modern High Energy Physics (HEP) experiments is pushing the research in the field of silicon radiation detectors to new challenging frontiers. Due to the high radiation doses foreseen for the inner tracking layers, radiation hard detectors must be designed and tested in order to provide reliable particle detection up to fluences in the order of 10^{16} 1-MeV equivalent neutrons per square centimeter ($\text{n}_{\text{eq}}\text{cm}^{-2}$). At the same time these devices must be fast and less power consuming than the older ones. For these reason several R&D projects in the field of silicon radiation detectors have been launched in the past years, mainly focusing on the upgrades of the experiments at the Large Hadron Collider (LHC) at CERN, Geneva, Switzerland [1]. The main macroscopic consequences of radiation-induced defects in the detector bulk are: (i) changes in effective doping concentration, mainly with introduction of acceptor-like defects that lead to an increase of the full depletion voltage, (ii) higher leakage currents due to the creation of generation/recombination centers, and (iii) decrease of the charge collection efficiency due to carrier trapping [2]. The overall consequence of this damage is a strong reduction in the signal to noise ratio that can severely reduce the tracking capabilities. To counteract these effects different strategies are possible [3]: i) material engineering, i.e., using as a substrate either non standard silicon (e.g., Magnetic Czochralsky, epitaxial, etc.) or diamond, that are intrinsically more resistant to radiation damage; ii) device engineering, which consists

in designing detectors with geometrical configurations that allow for lower signal degradation after irradiation. One of the most promising approaches to achieve radiation hard silicon detectors is the so-called 3D-architecture proposed by Parker and collaborators in the mid '90s [4]. In 3D detectors the electrodes have a columnar shape and are etched perpendicularly to the wafer surface, so as to penetrate in the wafers for their entire thickness. In this way the distance between electrodes is not bound to the thickness of the wafer anymore (that is the case for standard silicon detectors made by the planar process) and the designer is free to arrange electrodes in the most convenient way (the distance between the electrodes can be as short as few tens of microns). This results in decoupling the distance between the electrodes from the active volume of the sensor: as a consequence, low operating voltages (less than 10 V before irradiation, at most 200 V after irradiation), fast response times, and strong reduction of charge trapping effects after irradiation are obtained [5]. Another important feature of 3D detectors is their sensitivity up to a few microns away from the physical edge, allowing for more efficient area coverage on wide surfaces and lower material budget [6]. Besides all these advantages, 3D detectors have some disadvantages: in particular, the fabrication process is more complicated than a standard silicon detector process, the capacitance is higher and their response is not completely uniform because of the electrodes, that are not fully efficient, and of the presence of some low field regions. In order to develop 3D silicon detectors for the ATLAS upgrade the so-called ATLAS 3D sensor collaboration [7] was formed, involving many research centers and institutes from all over the world. Among the technological approaches considered for 3D fabrication, besides the original one developed at Stanford [8],

*Corresponding author, now at University of Geneva (CH).
Email address: alessandro.larosa@cern.ch (A. La Rosa)

are also simplified architectural implementations. One of them, relevant to the detectors considered in this work, is the so-called 3D Double sided Double Type Column (3D-DDTC) concept, independently proposed by FBK, Trento, Italy [9] and by CNM, Barcelona, Spain [10] with the aim of reducing process complexity in view of medium volume productions. One of the main advantages of this approach is that it does not use a support wafer, thus avoiding the related steps of wafer bonding and final wafer removal and also easing detector assembly within a tracking system. Columns are etched from both wafer sides (n^+ from the top, p^+ from the bottom) and are not passing through the entire wafer thickness, so they only partially overlap. From TCAD simulations [9], it was predicted that the performance of 3D-DDTC detectors is comparable to that of standard 3D detectors if the column overlap is a significant fraction of the wafer thickness, whereas it can be degraded if column thicknesses are not optimized, which is the case for the first prototypes fabricated at FBK and considered in this paper. Hence, the radiation hardness should be carefully studied in order to obtain useful information for the design and technology optimization. These devices were previously tested both in laboratory [11] and in beam tests at CERN in pre-irradiation conditions [12], obtaining very good results. In order to study their radiation hardness, different irradiation campaigns were conducted, and irradiated detectors were measured again in a test beam at CERN [13] and in laboratory. In this paper we report on selected results from functional characterization with radioactive sources conducted in laboratory on these 3D-DDTC detectors. Numerical simulations are also used to gain better insight into experimental results. The paper is organized as follows: Section 2 gives a brief description of devices under test and summarizes the two proton irradiation campaigns; Section 3 describes and discusses post-irradiation measurement results also comparing them with pre-irradiation results; Section 4 reports numerical simulation results and compares them to the measurements. Conclusions follow.

2. Experimental

2.1. Sensor description

The sensors under test are 3D-DDTC detectors fabricated at FBK on 4", 200 μm thick, p-type, FZ silicon wafers. As previously stated, in these devices columns are etched from opposite sides of the wafer and are not completely passing through the silicon bulk [8]. At the time of fabrication of these sensors (2008) the Deep Reactive Ion Etching (DRIE) equipment was not yet available at FBK so the etching of the holes was commissioned to an external company (IBS, France) and problems related to the calibration of this step led to an un-even column depth (see Fig. 1 (left)). This problem translated in a relatively small column overlap, in the order of 90 μm , that of course is not ideal and could affect the device performance, especially after irradiation. The nominal column diameter is 10 μm . The surface insulation between n^+ electrodes on the front side is achieved by combined p-spray and p-stop implants [14], whereas all ohmic columns are shorted on the back side

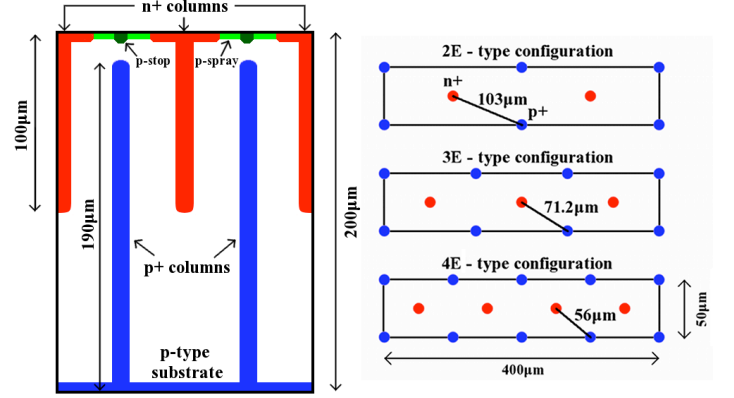


Figure 1: (left) Schematic cross-section of the sensors and (right) different pixel configurations.

by uniform p^+ diffusion and metal.

Devices under test are pixel detectors compatible with the FEI3 ATLAS read-out chip [15], and feature various layout options differing in the number of columns per pixel: 2E-type (two n^+ columns per pixel), 3E-type (three n^+ columns per pixel) and 4E-type (four n^+ columns per pixel). The number of ohmic columns per pixel also changes accordingly, and the inter-electrode distances are 103 μm , 71.2 μm , and 56 μm , respectively (see Fig. 1 (right)). Detectors were bump bonded to FEI3 ATLAS read-out chips at SELEX [16], Rome, Italy. The FEI3 chip was designed with radiation tolerant layout rules in a 0.25 μm CMOS technology. The maximum radiation dose that the chip can withstand is in the order of 50 Mrad. Detectors were designed to exactly match the geometry of the read-out channels of the chip which are 2880 in total and are arranged in a matrix of 160 rows per 18 columns (the pixel size is 400 μm x 50 μm). Each channel is composed by an analog and a digital part. The analog part integrates the sensor output current by means of charge sensitive preamplifier with constant current discharge, thus yielding a triangular pulse shape, which is fed to a discriminator along with a pre-set threshold. As a result, the width of the discriminator output signal, i.e., the Time Over Threshold (TOT) expressed in units of 40 MHz clock, is in first approximation proportional to the collected charge. Detailed explanation of the FEI3 operation can be found in [15].

2.2. Proton irradiation campaigns

In order to study the radiation tolerance of these sensors five devices were irradiated to two different proton fluences at two facilities: three samples at the Karlsruhe Institute of Technology (KIT) with a 25 MeV proton beam up to $1 \times 10^{15} \text{ n}_{\text{eq}} \text{ cm}^{-2}$ and two samples at CERN PS with a 24 GeV/c proton beam up to $2 \times 10^{15} \text{ n}_{\text{eq}} \text{ cm}^{-2}$ (see Table 1). The proton fluences were scaled to 1 MeV equivalent neutrons per square centimeter ($\text{n}_{\text{eq}} \text{ cm}^{-2}$) using the NIEL hypothesis with hardness factors of 1.85 and 0.62 for 25 MeV and 24 GeV protons, respectively. The uncertainty in the irradiation fluences is lower than 10 %. After the irradiation, the detectors were cooled to prevent annealing. However, the detectors had to be kept at room temper-

Module ID	Sensor Type	Fluence [$\text{n}_{\text{eq}}\text{cm}^{-2}$]	Particle	Facility
A	2E	1×10^{15}	25 MeV proton	KIT
B	3E	1×10^{15}	25 MeV proton	KIT
C	4E	1×10^{15}	25 MeV proton	KIT
D	2E	2×10^{15}	24 GeV proton	CERN PS
E	4E	2×10^{15}	24 GeV proton	CERN PS

Table 1: Overview of irradiated assemblies.

ature for a short time during handling and measurement setup, so that they experienced some annealing.

3. Functional lab-test measurements

Results from the electrical and functional characterization before irradiation of pixel detectors here considered is reported in [11], [17]. In this paper we will focus on measurements performed on irradiated devices and results of non-irradiated detectors will be recalled for a direct comparison (see a summary in Table 2). The sample characterization has been carried out by measuring: leakage current versus bias voltages, threshold, noise and response to radioactive γ - and β -sources. All measurements on irradiated devices were performed at -20°C in order to reduce leakage current and avoid reverse annealing effects.

Before irradiation detectors had leakage currents of a few hun-

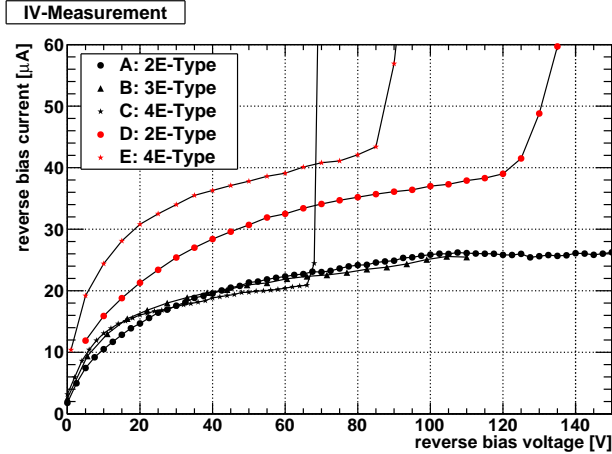


Figure 2: Overview of I-V curves from irradiated assemblies.

dred nA at room temperature and breakdown voltages between 60 V and 70 V. After irradiation, due to the displacement damage in silicon, the leakage current increased by several orders of magnitude, whereas, due to the increase of oxide charge concentration caused by ionizing radiation, the breakdown voltages were generally increased, sometimes well above 100 V, although results are not completely uniform. Breakdown voltage improvement after irradiation is typical of p-spray isolated planar structures [14], and also these 3D-DDTC sensors confirm the expectations. Fig. 2 shows an overview of leakage current versus bias voltage: the current values and trends are in

agreement with expectations, with different current levels corresponding to different irradiation fluences. Assemblies A, B and C were irradiated at $1 \times 10^{15} \text{ n}_{\text{eq}}\text{cm}^{-2}$ and show similar current values after irradiation (reaching about $25 \mu\text{A}$). A clear saturation at about 100 V can be observed for samples A and B, whereas sample C suffers from an earlier breakdown at about 65 V. Assemblies D and E were irradiated at $2 \times 10^{15} \text{ n}_{\text{eq}}\text{cm}^{-2}$ and reach currents of 35 to $40 \mu\text{A}$ (not yet fully saturated) before breakdown. The agreement between the leakage current damage constant ($\alpha \approx 5 \times 10^{-17} \text{ A/cm}$) extracted from these measurements and the generally accepted value of $4 \times 10^{-17} \text{ A/cm}$ [2] is good enough considering the uncertainties in the irradiation fluence, annealing conditions and temperature.

In order to evaluate the performance of the assemblies under test (sensor and front-end electronics), the system was calibrated aiming at a ToT of 60 units for a charge of 20 ke and a threshold of 3.2 ke. Threshold and noise measurements have been performed on each pixel based on S-cure fit function [18]. Table 3 summarizes the values of threshold and noise for the irradiated assemblies. Compared to values measured before irradiation (cf. Table 2), both threshold average and dispersion are very similar. Also noise values, expressed as equivalent noise charge (ENC), are only slightly different than before irradiation. As an example, Fig. 3 shows the ENC as a function of the volt-

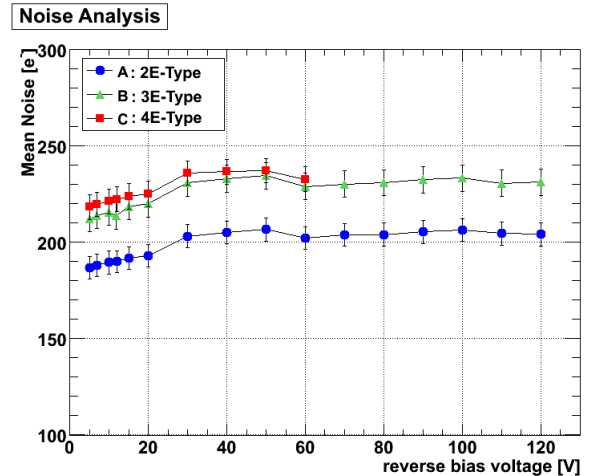


Figure 3: Equivalent noise charge as a function of bias voltages for irradiated assemblies A, B, and C.

age for sensors A, B, and C. The ENC curves are almost flat because, after irradiation to such a large fluence, the capacitance, that is the main factor for noise, is almost constant with bias due

Sensor type	I_{leakage} [nA]	$V_{\text{breakdown}}$ [V]	Threshold [e]	ENC [e]	^{241}Am 60-keV peak [ke]	^{90}Sr MPV peak [ke]
2E	250 - 300	60 - 70	3240 ± 54	197 ± 9	14.71	15.35
3E	250 - 300	60 - 70	3274 ± 51	206 ± 8	14.50	15.25
4E	250 - 300	60 - 70	3297 ± 56	227 ± 8	14.37	15.25

Table 2: Summary of typical results obtained from non-irradiated sensors. Except for $V_{\text{breakdown}}$, the parameters are obtained at a bias voltage of 35 V.

Module ID	Sensor type	Threshold [e]	ENC [e]	V_{test} [V]
A	2E	3265 ± 73	202.2 ± 11.6	60
B	3E	3153 ± 147	228.0 ± 14.0	60
C	4E	3268 ± 80	232.6 ± 13.3	60
D	2E	3018 ± 158	178.8 ± 18.4	110
E	4E	3307 ± 115	188.9 ± 17.3	120

Table 3: Threshold and noise values measured from irradiated assemblies.

to the very high resistivity of the substrate [20]. Different noise levels are observed, in agreement with the pre-irradiation case, because of the different capacitances characterizing the different column configurations (cf. Table 2). A direct comparison in the noise values before and after irradiation is difficult because of the different temperatures ($+20^\circ\text{C}$ vs -20°C): on one hand, the increase of leakage current in irradiated sensors would justify an increase in the noise in the order of tens of electrons rms [19], on the other hand this increase might well be compensated by the much lower temperature used for measurements after irradiation. Limiting the comparison to the irradiated samples, it might be puzzling that those irradiated at $2 \times 10^{15} \text{ n}_{\text{eq}}\text{cm}^{-2}$ (samples D and E) show lower noise than those irradiated at $1 \times 10^{15} \text{ n}_{\text{eq}}\text{cm}^{-2}$ (samples A, B, and C), but it should be noted that this difference might be due to the radiation damage to the electronics rather than to the sensors: in fact, for the 24-GeV proton irradiation a Total Ionizing Dose (TID) of about 54 Mrad has been estimated, whereas the estimated TID is 144 Mrad for 25-MeV proton irradiation. The former TID value is close to the one for which the FEI3 chip has been designed (50 Mrad), whereas the latter is much higher and could be responsible for a degradation in the chip noise performance.

Charge collection mechanisms were studied by means of an ^{241}Am γ -source and a ^{90}Sr β -source, comparing the results with those obtained before irradiation (cf. Table 2). For ^{241}Am measurements, the self-triggering capabilities of the system were exploited, whereas for ^{90}Sr measurements the trigger was taken from a scintillator placed behind the devices under test.

Table 4 summarizes the results of ^{241}Am γ -source measurements for the three sensors irradiated at $1 \times 10^{15} \text{ n}_{\text{eq}}\text{cm}^{-2}$ (data are not available for samples D and E). Before irradiation (cf. Table 2) a mean charge value of about 14.5 ke without clustering had been obtained with an applied reverse bias of 35 V. This charge corresponds to the energy peak at 60 keV, in agreement with theoretical expectations within the uncertainty due to the calibration process, which was estimated to be in the order of 10-15 %. Looking at Table 4, it is possible to notice that after irradiation, samples B and C yield a value of collected charge comparable to the value before irradiation, whereas sample A

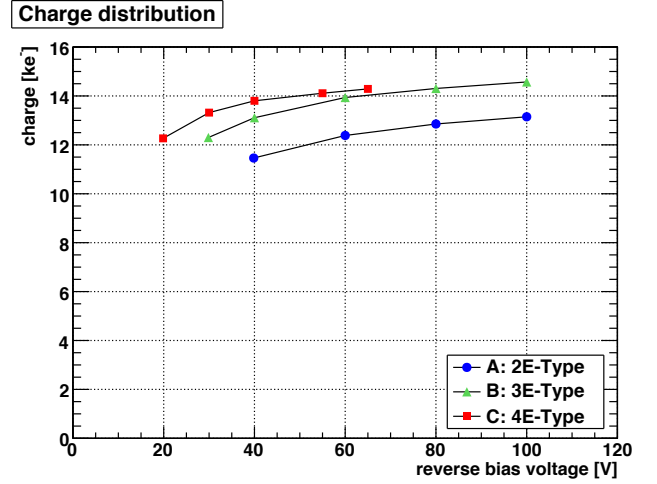


Figure 4: Mean peak (60-keV) of the collected charge for ^{241}Am source measurements as a function of reverse bias voltage in all irradiated samples.

(2E-type) shows lower collected charge. This can be ascribed to the longer distance between the n^+ and p^+ electrodes in sample A, which results in higher trapping probability. The importance of the column geometry is confirmed by results in Fig. 4, which shows the mean charge values as a function of the bias voltage for the three samples. Sensor C (4E-type) reaches roughly the same maximum charge as sensor B (3E-type), but at a lower voltage, owing to a lower distance between electrodes. Even higher voltage is necessary to have a significant charge collection in sensor A, that also tends to saturate at a lower charge value. An example of ^{241}Am spectrum measured with sample C is shown in Fig. 5. The main peak corresponding to the 60-keV photons is distorted with a tail towards lower charge values, that can be attributed to the absorption of photons in regions with lower electric field, for which the charge collection is not fully efficient.

Table 5 summarizes β -source measurements for all irradiated detectors biased at the highest possible voltage. Fig. 6(a) shows the pulse height spectrum in response to a ^{90}Sr β -source in the 4E sensor irradiated with protons at $1 \times 10^{15} \text{ n}_{\text{eq}}\text{cm}^{-2}$ (sample

Module ID	Sensor type	^{241}Am 60-keV peak [ke]	V_{test}
A	2E	12.8	80
B	3E	14.5	100
C	4E	14.3	65

Table 4: Collected charge from the assemblies irradiated at $1 \times 10^{15} \text{ n}_{\text{eq}}\text{cm}^{-2}$ exposed to ^{241}Am source.

Module ID	Sensor type	^{90}Sr MPV peak [ke]	V_{test}
A	2E	10.1	120
B	3E	11.6	100
C	4E	10.6	60
D	4E	9.0	160
E	4E	9.8	120

Table 5: Collected charge from all irradiated assemblies exposed to ^{90}Sr source.

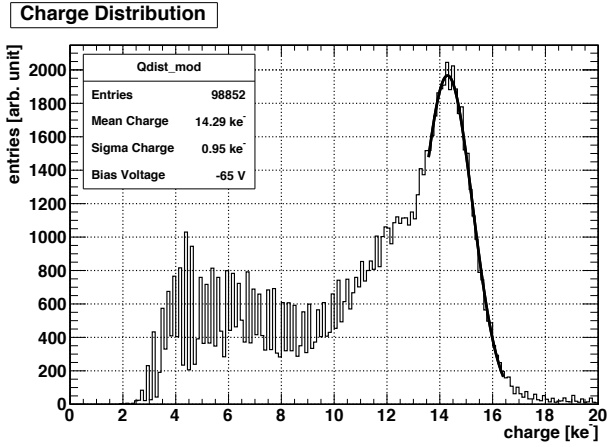


Figure 5: ^{241}Am spectrum measured with a 4E-type detector (sample C) irradiated with protons at $1 \times 10^{15} \text{ n}_{\text{eq}}\text{cm}^{-2}$ and reverse biased at 65 V.

C). The distribution is related to all clusters, and charge values in excess of 7 ke have been fitted with a Landau function, which is also shown in the figure. The most probable value (MPV) of the collected charge is 10.65 ke, whereas it was about 15 ke before irradiation (cf. Table 2). Thus, the degradation in charge collection is more pronounced than that observed for the ^{241}Am γ -source measurements. This is generally the case for all the irradiated assemblies, as can be seen from the values in Table 5. The reason for this behavior is related to the different ways charge is generated inside the sensors: while every γ -ray in silicon can be absorbed at different depths and the released charge is localized in a region of a few cubic micrometers, β particles traverse the whole bulk thickness releasing charge along the entire track. This means that, if the device is not fully depleted, part of the charge released by a β particle will be generated in a non depleted region and therefore almost completely lost (due to recombination). On the contrary, for all the γ -rays absorbed in the region where columns overlap the generated charge will be collected also after irradiation, except for the case where the inter-electrode distance is too large,

because of trapping. Assemblies irradiated at $1 \times 10^{15} \text{ n}_{\text{eq}}\text{cm}^{-2}$ perform reasonably well, considering that the applied voltage is high enough to achieve lateral depletion between the columns, but a non negligible fraction of the devices at the bottom is not depleted, thus causing charge loss (this effect will be better explained in the following with the aid of TCAD simulations). Samples irradiated at $2 \times 10^{15} \text{ n}_{\text{eq}}\text{cm}^{-2}$ show further degradation of the collected charge with respect to those irradiated at $1 \times 10^{15} \text{ n}_{\text{eq}}\text{cm}^{-2}$, due to stronger trapping effects. Nevertheless, the collected charge is still reasonably good because of the higher bias voltage that could be applied to these sensors before they reached breakdown, which allowed lateral depletion between columns to be achieved both for the 2E and the 4E configurations. Again, the 4E sample collects more charge than the 2E one at a lower voltage owing to the shorter distance between the electrodes. The cluster size distribution for sample C is also shown in Fig. 6(b). Most events ($\sim 80\%$) are cluster size 1, the remaining part ($\sim 20\%$) are cluster size 2. This distribution can be explained taking into account that β particles reaching the sensor are not all perpendicular to the surface due to the geometry of the collimator. The angle distribution was found to span from 90° to 84.29° . Although in 3D sensors the electric field distribution provides a sort of self-shielding effect in each pixel, in case particle hits are not perpendicular to the surface the probability of charge sharing between two adjacent pixels becomes non negligible.

The performances of some of the irradiated devices considered in this paper were also tested with a $120 \text{ GeV}/c \pi^+$ beam at CERN SPS in June 2010. The aim of this test was to study tracking efficiency, charge sharing and cluster size. A detailed description of the obtained results can be found in [13]. It should be noticed that both the values of the collected charge and the cluster size distributions are in very good agreement with those measured in laboratory.

The MPV of the collected charge reported in Table 5 are relevant to the highest possible bias voltage. The variation of the MPV with the bias voltage is also of interest to better understand the behavior of these sensors. Fig. 7 summarizes data for all the irradiated assemblies. As expected, the collected charge

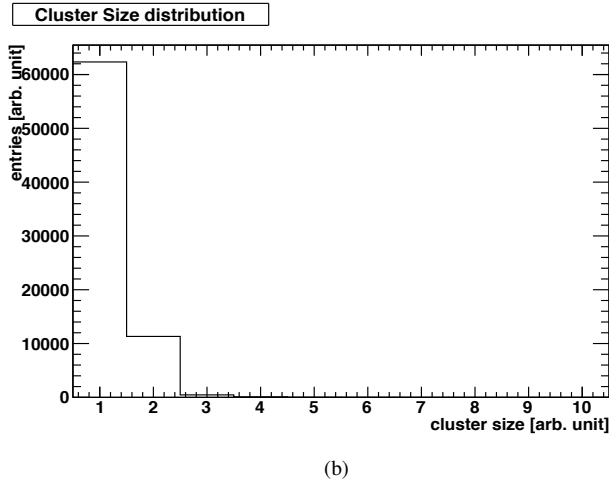
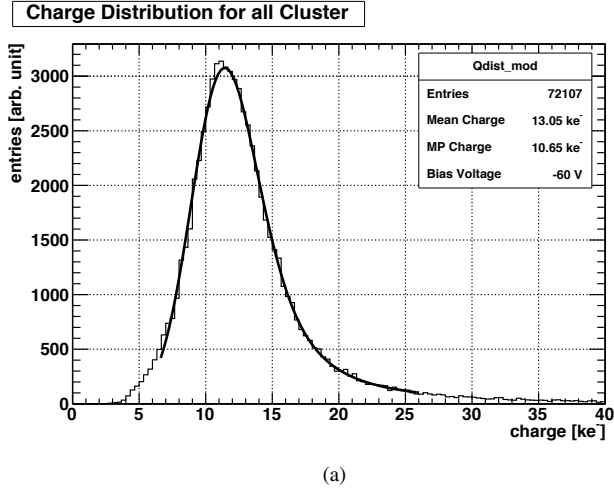


Figure 6: Results for tests with ^{90}Sr source on a 4E-type detector (sample C) irradiated with protons at $1 \times 10^{15} \text{ n}_{\text{eq}}\text{cm}^{-2}$ and biased at 60 V: (a) pulse height distribution, and (b) cluster size distribution.

increases with the applied voltage in agreement with the larger depleted volume within the sensors. A part from sensor A, for which trapping effects are more severe as also observed with γ -rays, charge values are not yet completely saturated in the considered voltage range. In agreement with the decreasing distance between the electrodes, the same value of collected charge is observed at a lower voltage in 4E samples with respect to 3E and 2E ones. Samples irradiated at $2 \times 10^{15} \text{ n}_{\text{eq}}\text{cm}^{-2}$ of course need a higher bias voltage to reach a sufficient charge collection efficiency, and maximum values are slightly lower due to trapping.

4. TCAD simulations

In order to better understand the experimental results, numerical simulations were performed with TCAD tools from Synopsys [21]. Simulations were focused on devices measured with ^{90}Sr β -source, in order to limit the computational load and reduce the simulation time. Results were obtained for every detector type (2E, 3E, and 4E) but in this paper we only report on

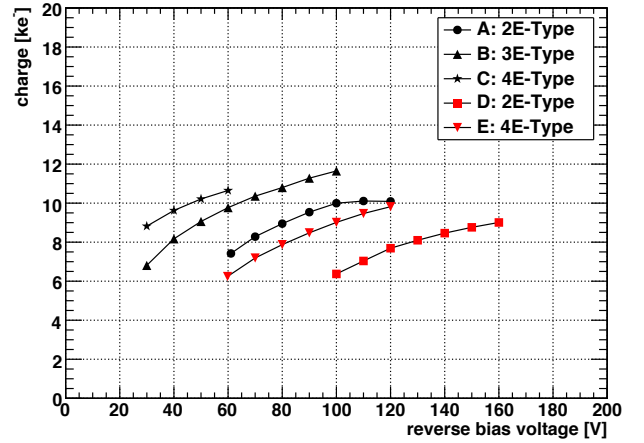


Figure 7: Most Probable Value (MPV) of the collected charge for ^{90}Sr source tests as a function of reverse bias voltage in all irradiated samples.

a 4E-type detector irradiated at $1 \times 10^{15} \text{ n}_{\text{eq}}\text{cm}^{-2}$ for the sake of conciseness. Similar considerations apply to the other sensors. Simulations were performed at different bias voltages. Moreover, the two extreme values of particle incidence angle were tested (90° and 84.29°). To this purpose, since the probabil-

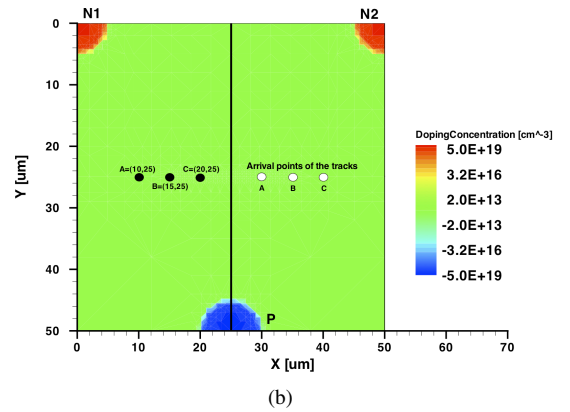
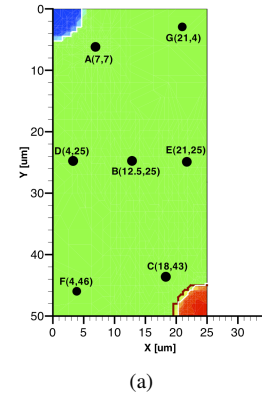


Figure 8: Front view of simulated structures: (a) structure for cluster size 1 simulations with different particle hit points, and (b) structure for cluster size 2 simulations with different particle hit and arrival points (track angle 84.29°).

ity of charge sharing is strictly related to the inclination of the particle, two different structures were simulated: (i) a single cell including one n^+ column and one p^+ column, for a 90° hit angle (Fig. 8(a)) and (ii) two adjacent cells including two n^+ electrodes (related to adjacent pixels) and one p^+ column, for a 84.29° hit angle (Fig. 8(b)). Moreover, to have a better understanding of the behavior of the detectors, different particle hit points were tested and the results were combined as explained below.

Particle hit was simulated using the Heavy-Ion model available in the simulator: the released charge was 80 electron-hole pairs per micron and the spatial distribution was Gaussian in a region of one micrometer diameter around the track. The radiation damage was modeled using the Perugia trap model [22] modified as described in [23].

Transient simulations were performed from 0 to 100 ns; the high leakage current was subtracted from the output current and a numerical integration was performed in order to extract the total collected charge for each simulation. In order to decide if an event was good or not, the collected charge after 20 ns was observed and, if the value was above the threshold (3200 e), the hit was considered valid and the value at which the integral saturated was taken as the total charge collected in that event. In simulations of the structures consisting of two adjacent cells from different pixels, we repeated this procedure for both n^+ columns.

Since measurements showed that 80 % of the events are cluster size 1 while 20 % are cluster size 2, simulation results were combined using the following equation:

$$Q_{all-cluster,sim} = 0.8 \times Q_{CS1} + 0.2 \times Q_{CS2} \quad (1)$$

where Q_{CS1} is the total collected charge for cluster size 1 events while Q_{CS2} is the total collected charge for cluster size 2 events (the sum of the charge collected on two adjacent pixels). Since the simulation does not take into account delta rays, these results were compared with the measured mean charge and a very good agreement was found (see Fig. 9). In order to gain a better insight into the charge collection process, several cuts were extracted from the simulations results showing different electrical quantities, among them the electric field, Shockley-Read-Hall (SRH) recombination, electron density, and hole density for different bias voltages and different depths inside the device. In particular, two voltages (20 V and 60 V) were chosen as representative of low-bias and high-bias conditions, and the cuts were extracted from two separate regions, one in the part of the sensor where columnar electrodes overlap ($z = 50 \mu\text{m}$) and the other in the non-overlap region ($z = 150 \mu\text{m}$). This was done because these two regions of the device behave in completely different way one to the other, especially after irradiation.

The above-mentioned quantities, relevant to a time instant 0.5 ns after the particle hit the device perpendicularly to the wafer surface (point E in Fig. 8(a)), are shown in Figs. 10 - 13. Looking at Fig. 10, it is clear that for both bias voltages the electric field is strong only in the overlap region (with a much higher absolute value for 60 V bias), whereas it is very weak in the bottom part of the sensor. From Fig. 11, it is

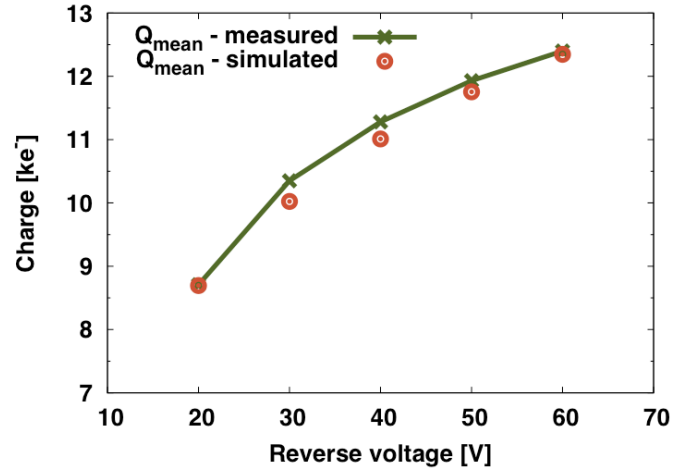


Figure 9: Comparison between measured (green cross-shaped) and simulated (red dots) mean collected charge as a function of reverse bias voltage for a sensor C (4E-type) irradiated at $1 \times 10^{15} \text{ n}_{eq} \text{ cm}^{-2}$.

possible to confirm that SRH recombination is negligible in the overlap region, whereas it significantly affects those carriers generated by the impinging particle in the non-overlap region. Both the distributions of the electric field distribution and the SRH recombination can be explained considering the way the depletion region extends inside this type of devices: full depletion occurs at relatively low bias voltages in the overlap region, whereas much larger voltages would be required to fully deplete the bottom part of the device.

Given that part of the charge generated by the impinging particle is lost because of recombination, it is important to understand how the rest of the carriers move inside the device and how they contribute to the signal formation. Figs. 12 and 13 show the electrons density and hole density distributions for the same biasing conditions, depths and time instant. From the electron density point of view, it is clear that carriers generated in the top part of the detector are collected almost immediately owing to the strong electric field. The effect of the bias voltage is clearly visible because the electrons are collected faster at 60 V than at 20 V in this region. The situation in the bottom part of the device is different: the electric field is much weaker and carriers must drift (or even diffuse in non depleted regions) both laterally and vertically toward the tip of the n^+ column. Since distances are longer and the field is weaker, carriers in this region will require more time to be collected, drastically increasing the probability of being trapped or recombining. The minor changes in the bottom part of the device between 20 V and 60 V indicate that the device has not reached an optimal working point. The previous considerations can also be applied to what happens for the hole density in Fig. 13. Again, holes are collected much faster in the overlap region than in the bottom region. Another aspect to highlight is that, for a bias voltage of 20 V, the hole density at $z = 150 \mu\text{m}$ is very uniform and close to the bulk doping concentration, confirming that this region is not depleted.

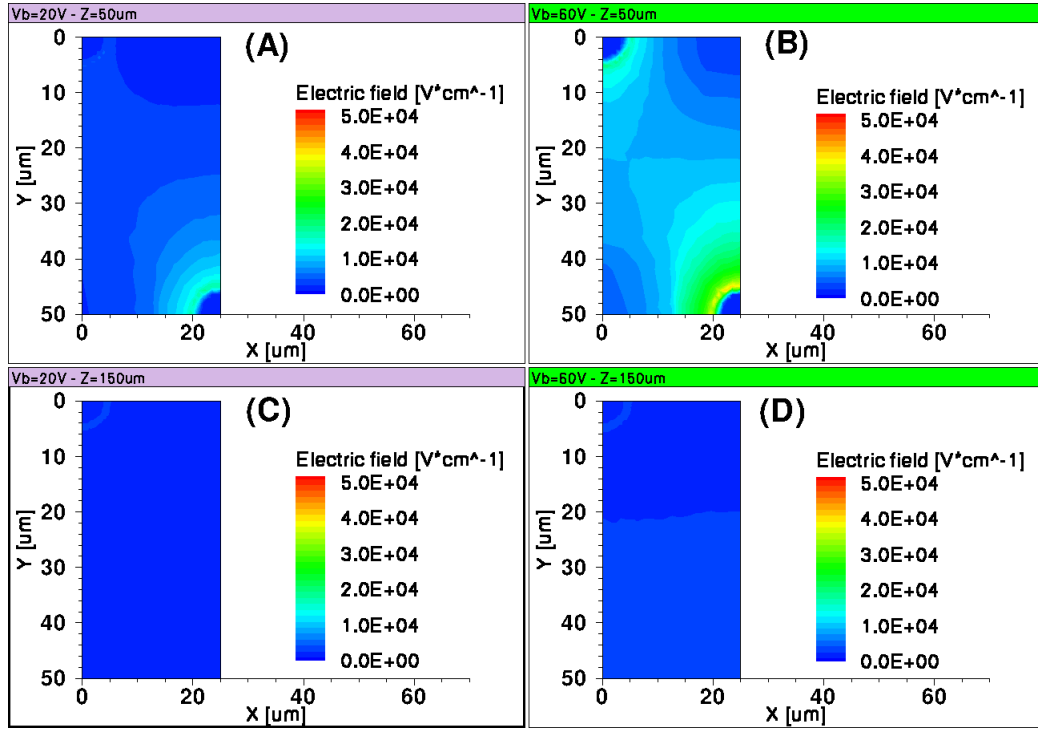


Figure 10: 2d cuts showing the electric field at two different depths (Z) and two bias voltages (V_b): (A) $Z = 50\mu\text{m}$, $V_b = 20\text{V}$; (B) $Z = 50\mu\text{m}$, $V_b = 60\text{V}$; (C) $Z = 150\mu\text{m}$, $V_b = 20\text{V}$; (D) $Z = 150\mu\text{m}$, $V_b = 60\text{V}$. Data are relevant to a time instant 0.5 ns after a particle hit the device perpendicularly to the wafer surface (point E in 8(a)).

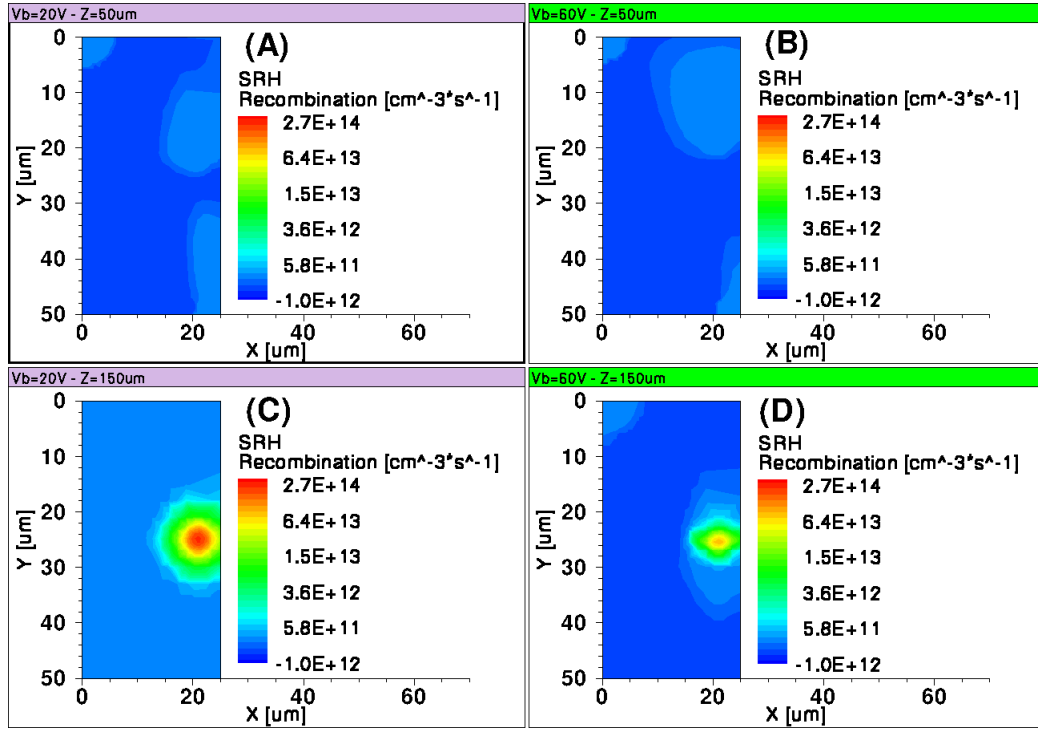


Figure 11: 2d cuts showing the SRH recombination at two different depths (Z) and two bias voltages (V_b): (A) $Z = 50\mu\text{m}$, $V_b = 20\text{V}$; (B) $Z = 50\mu\text{m}$, $V_b = 60\text{V}$; (C) $Z = 150\mu\text{m}$, $V_b = 20\text{V}$; (D) $Z = 150\mu\text{m}$, $V_b = 60\text{V}$. Data are relevant to a time instant 0.5 ns after a particle hit the device perpendicularly to the wafer surface (point E in 8(a)).

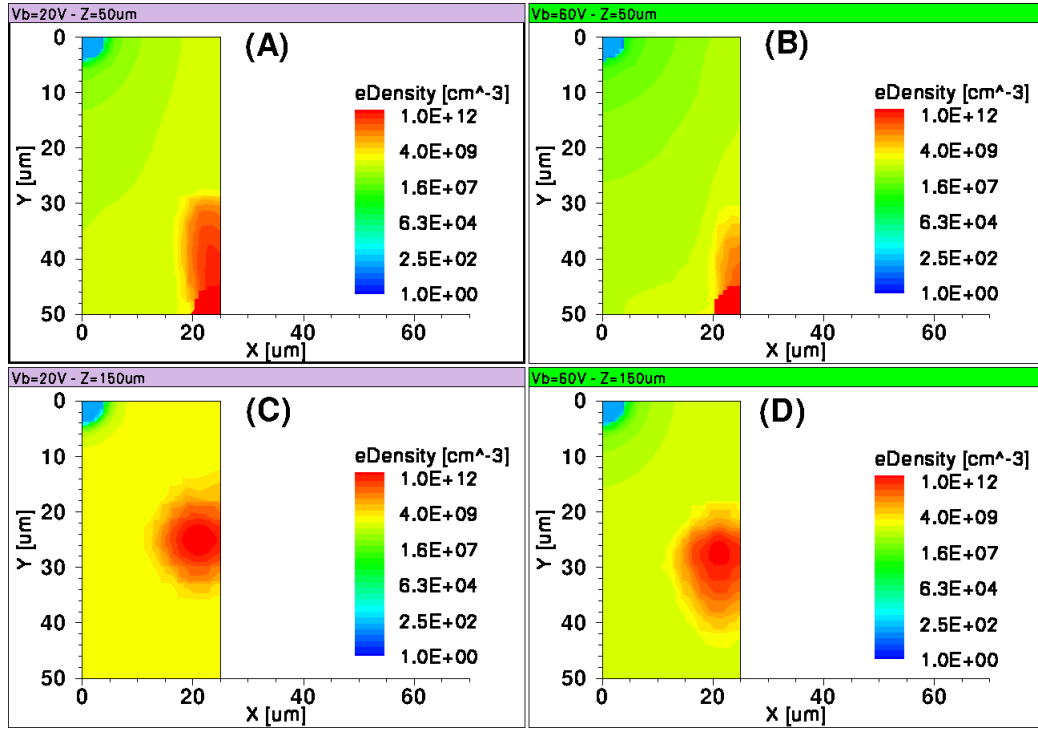


Figure 12: 2d cuts showing the electron density at two different depths (Z) and two bias voltages (V_b): (A) $Z = 50\mu\text{m}$, $V_b = 20\text{ V}$; (B) $Z = 50\mu\text{m}$, $V_b = 60\text{ V}$; (C) $Z = 150\mu\text{m}$, $V_b = 20\text{ V}$; (D) $Z = 150\mu\text{m}$, $V_b = 60\text{ V}$. Data are relevant to a time instant 0.5 ns after a particle hit the device perpendicularly to the wafer surface (point E in 8(a)).

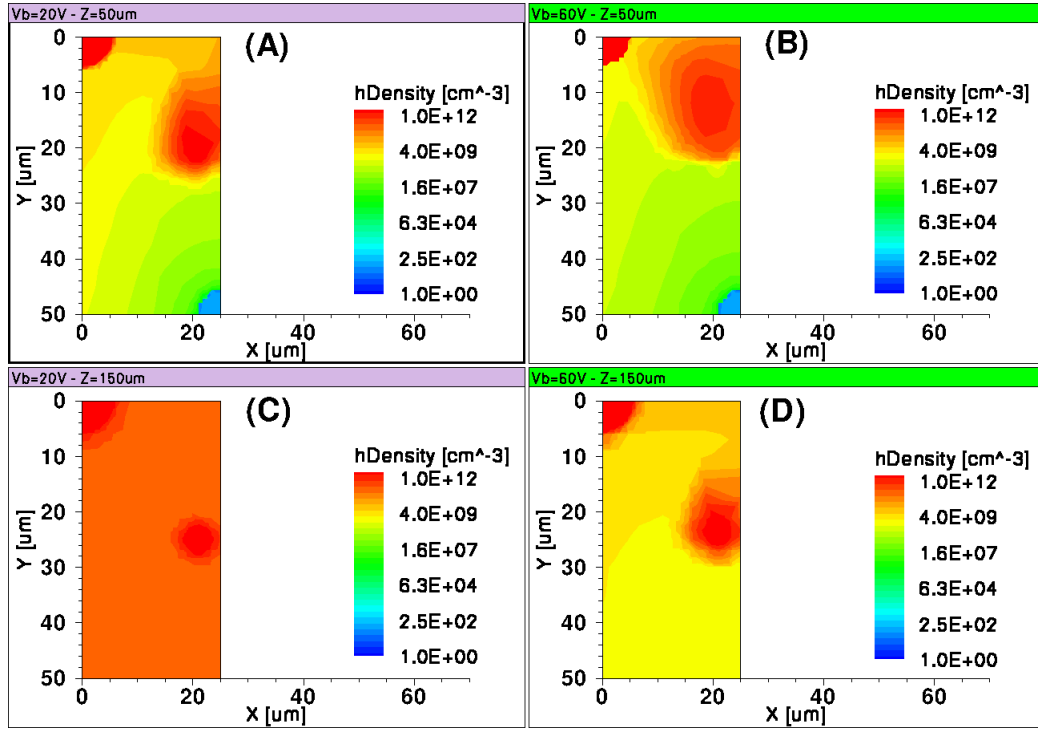
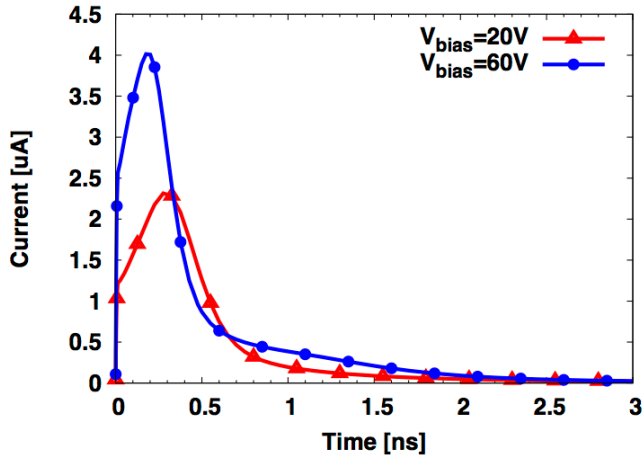
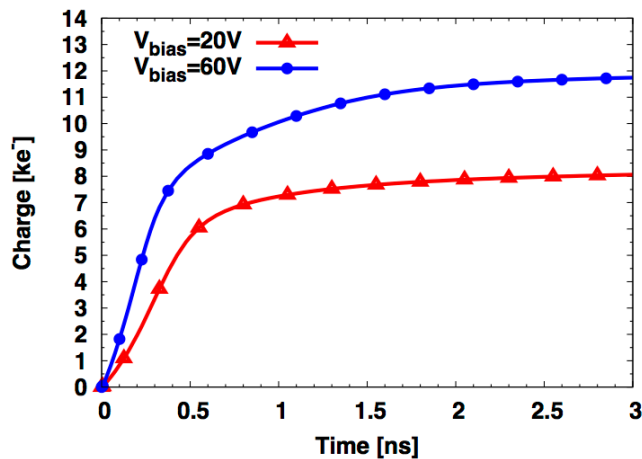


Figure 13: 2d cuts showing the hole density at two different depths (Z) and two bias voltages (V_b): (A) $Z = 50\mu\text{m}$, $V_b = 20\text{ V}$; (B) $Z = 50\mu\text{m}$, $V_b = 60\text{ V}$; (C) $Z = 150\mu\text{m}$, $V_b = 20\text{ V}$; (D) $Z = 150\mu\text{m}$, $V_b = 60\text{ V}$. Data are relevant to a time instant 0.5 ns after a particle hit the device perpendicularly to the wafer surface (point E in 8(a)).

The above analysis is in good agreement with simulation results in terms of transient output currents (Fig. 14(a)) and their time integrals (Fig. 14(b)) for the two considered biases (20 V and 60 V). As already mentioned, for higher bias voltages, electrons and holes in the overlap region suffer from less trapping and this translates into a pulse with higher amplitude and faster evolution thanks to the higher electric field (both electrons and holes generated in the overlap region concur in the formation of the fast peak). Apart from the difference in the peak amplitude and time, the clear difference in the tail of the two pulses should be stressed: while at 20 V (red curve) the tail is very short (1 to 1.5 ns), at 60 V (blue curve) the tail is longer and extends up to 3 ns. The change of the shape of the pulse tails is related to the fact that at 60 V of bias, the bottom part of the detector suffers from less recombination and the charge generated there also contributes to the output signal. Since the field in this region is weaker than in the top, the drift of the carriers will be slower, hence the presence of the long tail.



(a)



(b)

Figure 14: Simulated output currents at 20 V and 60 V bias (a) and corresponding time integrals (b).

5. Conclusion

We have reported on selected results from the functional characterization of irradiated 3D-DDTC pixel sensors fabricated at FBK. Sensors with different pixel configurations have been assembled with the ATLAS FEI3 read-out chip and irradiated with protons up to very large fluences. Experimental results from measurements carried out in the laboratory have been discussed and compared to those obtained before irradiation. As expected, the breakdown voltage was generally increased by a few tens of Volts with respect to the pre-irradiation values, allowing to operate the sensors at a bias voltage high enough to achieve at least lateral depletion between the columns. In all samples the noise figures are only slightly different from the pre-irradiation values despite the high leakage current. The peak of the collected charge in response to γ -rays from an ^{241}Am source is not significantly degraded with respect to the values obtained before irradiation, provided that the bias voltage is high enough to effectively counteract trapping in the top region of the devices where columns overlap. On the contrary, the most probable value of the collected charge for tests with β -particles from a ^{90}Sr source is found to be more sensitive to trapping, due to the lower charge collection efficiency from the bottom region of the devices, where columns do not overlap, in good agreement with TCAD simulations. Nevertheless, the signal efficiency, defined as the ratio of the MPV of the collected charge after irradiation and before irradiation, remains at acceptable levels: for the best sample irradiated at $1 \times 10^{15} \text{ n}_{\text{eq}}\text{cm}^{-2}$ it is about 76 % at 100 V, and for the best sample irradiated at $2 \times 10^{15} \text{ n}_{\text{eq}}\text{cm}^{-2}$ it is about 64 % at 120 V. These results are very encouraging since the tested samples have a rather short column overlap, less than one half of the sensor thickness. Hence, there is still wide room for performance improvement by etching deeper junction column depths. New 3D-DDTC sensors fabricated at FBK have indeed passing-through columns and are expected to be very radiation hard.

6. Acknowledgement

This work has been supported in part by Provincia Autonoma di Trento within Project MEMS2, and in part by the Italian National Institute for Nuclear Physics (INFN) within Projects TREDI (CSN5) and ATLAS (CSN1). We would like to thank G. Gariano, A. Rovani and E. Ruscino (INFN - Genova), F. Rivero (Torino University) for their precious help in system assembly and measurements; R. Beccherle (INFN Genova) for designing bump bonding mask; S. Di Gioia (Selex SI) for bump bonding process. We would like also to thank: A. Dierlamm (KIT) for proton irradiation in Karlsruhe (Germany), and M. Glaser (CERN) for proton irradiation at CERN PS (CH).

References

- [1] F. Gianotti, et al., Eur. Phys. J. C39 (2005) 293.
- [2] G. Lindstrom, M. Moll, E. Fretwurst, Nucl. Instrum. Methods A 426 (1999) 1.
- [3] CERN RD50 Collaboration. <http://www.cern.ch/rd50>
- [4] S. Parker et al., Nucl. Instrum. Methods A 395 (1997) 328.

- [5] C. Da Vià, et al., Nucl. Instrum. Methods A 604 (2009) 505.
- [6] C. J. Kenney, et al., IEEE Trans. Nucl. Sci. NS-48(6) (2001) 2405.
- [7] ATLAS Upgrade Document, <http://cern.ch/atlas-highlumi-3dsensor>
- [8] C. J. Kenney, et al., IEEE Trans. Nucl. Sci. NS-46(4) (1999) 1224.
- [9] A. Zoboli et al., IEEE Trans. Nucl. Sci. NS55(5) (2008) 2275.
- [10] G. Pellegrini, et al., Nucl. Instrum. Methods A 592 (2008) 38.
- [11] G.-F. Dalla Betta, et al., Nucl. Instrum. Methods A 636 Suppl.1 (2011) S15.
- [12] P. Grenier, et al., Nucl. Instrum. Methods A 638 (2011) 33.
- [13] A. Micelli, et al., Nucl. Instrum. Methods A 650 (2011) 150.
- [14] C. Piemonte et al., IEEE Trans. Nucl. Sci. NS-53(3) (2006) 1694.
- [15] I. Peric et al, Nucl. Instrum. Methods A 565 (2006) 178.
- [16] SELEX Sistemi Integrati, Roma, Italy. <http://www.selex-si.com>
- [17] A. La Rosa et al., Proceedings of Science PoS(RD09)032 (2009).
- [18] G. Aad et al., JINST 3 (2008) P07007.
- [19] L. Blanquart, et al., IEEE Trans. Nucl. Sci. NS-49(4) (2002) 1778.
- [20] R. Bates, et al., IEEE Trans. Nucl. Sci. NS-58(6) (2011) 3370.
- [21] Synopsys Advanced TCAD Tools. <http://www.synopsys.com/Tools/TCAD>
- [22] M. Petasecca et al., IEEE Trans. Nucl. Sci. NS-53(5) (2006) 2971.
- [23] D. Pennicard et al., Nucl. Instrum. Methods A 592 (2008) 16.